

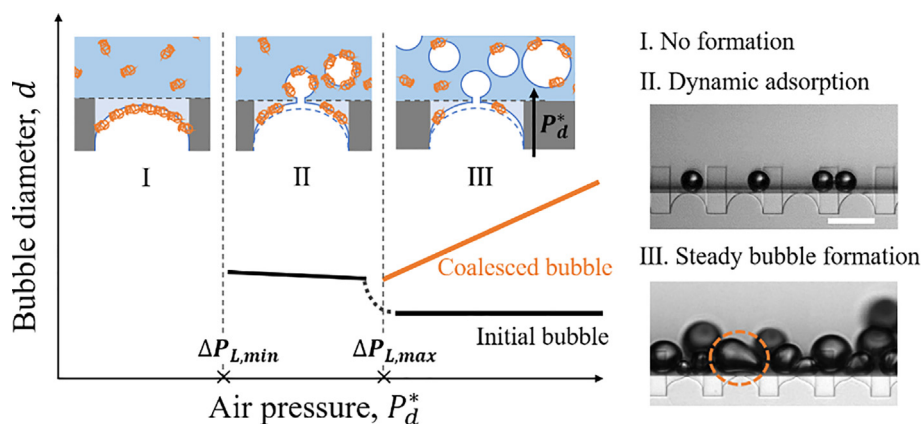


## Regular Article

Effects of dynamic adsorption on bubble formation and coalescence in partitioned-EDGE devices <sup>☆</sup>Boxin Deng, Karin Schroën, Jolet de Ruiter <sup>\*</sup>

Wageningen University, Food Process Engineering Group, Bornse Weiland 9, 6708 WG Wageningen, The Netherlands

## GRAPHICAL ABSTRACT



## ARTICLE INFO

## Article history:

Received 11 March 2021

Revised 31 May 2021

Accepted 2 June 2021

Available online 4 June 2021

## Keywords:

Bubble formation dynamics

Coalescence

Microfluidics

Pressure-driven flow

Protein stabilization

Overlapping time scales

Empirical coalescence model

## ABSTRACT

**Hypothesis:** Dynamic adsorption effects can play a crucial role in bubble formation and stabilization. We hypothesize that microfluidic tools provide direct insights to these effects, and that the final bubble size depends on the intersection of time scales for bubble formation *versus* adsorption of proteins.

**Experiments:** We use a microfluidic device to study Laplace pressure-driven formation of bubbles that are stabilized by whey proteins. Bubble behavior is studied as a function of the pressure difference imposed across the pores ( $P_d^*$ ), and thus the bubble formation time ( $\tau$ , ranging from  $\mu\text{s}$  to  $\text{s}$ ), using high-speed recordings, quasi-static pressure arguments and a semi-empirical coalescence model.

**Findings:** We observe two distinct bubble formation regimes, delimited by the pressure difference required to initiate bubble formation in pure water,  $P_d^* = 1400$  mbar. When  $P_d^* < 1400$  mbar, protein adsorption is a requisite to lower the surface tension and initialize bubble formation. Individual bubbles (fixed  $d_0 \sim 25 \mu\text{m}$ ) are formed slowly with  $\tau \gg 1$  ms. When  $P_d^*$  exceeds 1400 mbar, bubbles (fixed  $d_0 \sim 16 \mu\text{m}$ ) experience no adsorption lag and thus are formed at steeply increasing frequency, with  $\tau < 1$  ms. Interaction between these bubbles causes finite coalescence to a diameter  $d_{coal}$  that increases for lower  $\tau$ . A minimum time of 0.4 ms is needed to immediately stabilize individual bubbles. Our study provides a promising microfluidic tool to study bubble formation and coalescence dynamics simultaneously.

© 2021 The Author(s). Published by Elsevier Inc. This is an open access article under the CC BY license (<http://creativecommons.org/licenses/by/4.0/>).

<sup>☆</sup> Electronic supplementary information (ESI) available.

<sup>\*</sup> Corresponding author.

E-mail address: [jolet.deruiter@wur.nl](mailto:jolet.deruiter@wur.nl) (J. de Ruiter).

## 1. Introduction

Microfluidic devices are used to generate individual bubbles and droplets at microscale pores, yielding high monodispersity and a tight control over volume and production frequency. Broadly, microfluidic geometries belong to the category of either shear-based or spontaneous devices. In shear-based devices such as flow-focusing [1–4] and *T*-junction [5–8], a bubble or droplet is sheared off from the supply thread (gas or liquid) by a contacting flow. This type of devices have high sensitivity to flow conditions (i.e. flow rate ratios), which, on one hand, allows to carefully tune the bubble size and the bubble formation frequency – though they are interrelated [1]. On the other hand, flow sensitivity poses a drawback in upscaling and steady operation of these devices – which is particularly challenging for bubble formation due to air compressibility [9]. To increase scalability, spontaneous devices with a sudden expansion in channel height (and thus being three-dimensional) have been developed [10,11]. In these devices bubbles or droplets form spontaneously, not by shear but by a sudden decrease in Laplace pressure of the interface – from a confined, strongly-curved meniscus to a less-curved bubble or droplet. The continuous phase flow is then only needed for clearing the channel exit. As a result, spontaneous devices are capable of resisting fluctuations in flow, and thus show stable operation over a wider range of dispersed phase pressures or flow rates. These geometries are either straight-through microchannels with constant channel width [12,13], or also include a wider plateau or terrace to further manipulate droplet formation and the pressure stability. This plateau can be placed downstream of the channel just before the vertical step [14–20], or, inversely, the wider plateau can be partitioned into individual channels (pores) just before the vertical step, like in the so-called partitioned Edge-based Droplet GEneration (partitioned-EDGE) device [21].

So far, spontaneous devices have been mostly used for studying emulsification – droplet formation. Depending on the dispersed phase flow rate, droplets (or bubbles) are formed via a so-called ‘dripping’ or ‘jetting’ mechanism [12,16,22], or via two stable regimes [21] in which droplet formation in the second regime is dominated by the droplet–droplet interactions [23]. Typically, as an individual droplet grows, the neck constricted within the channel contracts until finally the break-up is triggered. When the flux of dispersed phase out of the neck (forming the droplet) exceeds the supplying flux through the channel, the neck thins and breaks, and a droplet is formed [24,25]. Alternatively, when the neck shrinks to a width smaller than the channel’s height, it thins following a Rayleigh-Plateau type instability and breaks [26]. In either of these cases, the backflow of the continuous phase towards the location of the neck is expected to stretch the neck and facilitate its break-up, thus playing a crucial role in droplet formation [27]. However, although the droplet formation mechanism has been extensively studied, and bubble formation shares many features with droplet formation, dynamics of bubble formation is still under investigation and holds for example additional effects of air compressibility [22].

In spontaneous devices, interfacial tension provides the dominating force for the transformation of the constricted dispersed phase into droplets (or bubbles) [11]. The (few) studies of bubble formation in spontaneous devices are typically performed under conditions of constant, equilibrium surface tension [15,18,28], making use of very high loading of fast-adsorbing low-molecular weight surfactants like SDS or Tween 20, and relatively slow bubble formation. In this limiting case, the formed bubbles are either stable, or any coalescence after formation is simply neglected. However, in real foaming processes the dynamic adsorption of surfactants to the interface is a crucial stage upon shear-induced frag-

mentation of bubbles [29] and has two important effects. First, adsorption of surfactants to a fresh interface lowers the surface tension which can influence both the initialization of bubble formation [30], and the bubble size [15]. Second, sufficient surface coverage prevents coalescence of bubbles [31,32] and thus slows down the increase of bubble size over time. In the production of food foams, whey proteins are commonly used as the surfactant. Compared to the above-mentioned low-molecular weight surfactants (e.g. SDS), protein adsorption slightly differs in interfacial behavior. On one hand, once adsorbed at the interface, proteins undergo structural re-arrangement and thus form a viscoelastic interfacial film [33], providing protein-covered bubbles a particularly high stability [29]. On the other hand, the adsorption of proteins is typically slower, even though it is accelerated due to enhanced mass transport in microchannels [33–36]. As is concluded by Chen and co-authors [37], it is crucial to measure interfacial dynamics at relevant length and time scales. In the case of bubbles, bubble formation may happen at a micro- [18] or milli- [15,28] second time scale in spontaneous devices; while an upper estimate of the time scale of whey protein-stabilization of bubbles is given by Muijlwijk et al. [32]. They have shown that bubbles are stable against coalescence after allowing a (fixed) 100 ms adsorption time in presence of 1% wt.  $\beta$ -Lactoglobulin, which is the major component of whey protein isolate. Thus, the time scales of bubble interface creation and protein adsorption possibly overlap. Dynamic adsorption effects are expected to play a crucial role in bubble formation and stabilization as mentioned above, yet they are not fully understood at relevant time scales.

In this work, we study bubble formation in a partitioned-EDGE device with whey proteins as the surfactant. By varying the pressure difference across the pores between the dispersed and continuous phases, and thus the bubble formation frequency, we study a wide range of time scales of bubble formation. We observe the co-existence of bubble formation and finite bubble coalescence. Accordingly, we use a pressure analysis to explain the role of dynamic protein adsorption on the initiation of bubble formation, and use an empirical coalescence model to describe the successive bubble coalescence. We thus elucidate the role of dynamic adsorption of proteins within (sub)milliseconds using microfluidics.

## 2. Experimental

We study the formation of air bubbles in aqueous (Milli-Q, Merck Millipore) solution of 5% wt. whey protein isolate (BiPro, 97.5% purity, Agropur, Canada), filtered with 0.22  $\mu\text{m}$  PES filters (Merck, Germany). Bubbles are formed in a partitioned-EDGE microfluidic glass chip, which was previously designed in our group and produced using deep reactive ion etching technique by Micronit Microtechnologies B.V. (Enschede, the Netherlands). The design consists of relatively deep ( $H = 175 \mu\text{m}$ ) dispersed (air) and continuous (aqueous) phase channels, connected by five shallow plateaus of 500  $\mu\text{m}$  width ( $W$ ), 200  $\mu\text{m}$  length ( $L$ ) and 1  $\mu\text{m}$  height ( $h$ ), as shown in Fig. 1. The five plateaus operate more-or-less independently, with the first one being focused on in this study. The end of the plateau is partitioned into eight parallel pores of 40  $\mu\text{m}$  width ( $w$ ) and 20  $\mu\text{m}$  length ( $l$ ). The distance between the centers of two pores is 60  $\mu\text{m}$ . The pores have the same height as the shallow plateau ( $h = 1 \mu\text{m}$ ). The extreme shallowness of the plateau (and the pores) is a key feature influencing operation of the device, via both high Laplace pressure  $\Delta P_L \sim \gamma/h$  (where  $\gamma$  is the surface tension between air and continuous phases) of the meniscus in the pore, and high hydrodynamic resistance  $\mathcal{R} \sim 1/h^3$ . Here, the hydrodynamic resistance of the pore itself can be calculated by  $\mathcal{R} = \frac{12\eta l}{h^3 w [1 - 0.630(h/w)]}$ , with  $\eta$  the viscosity of air

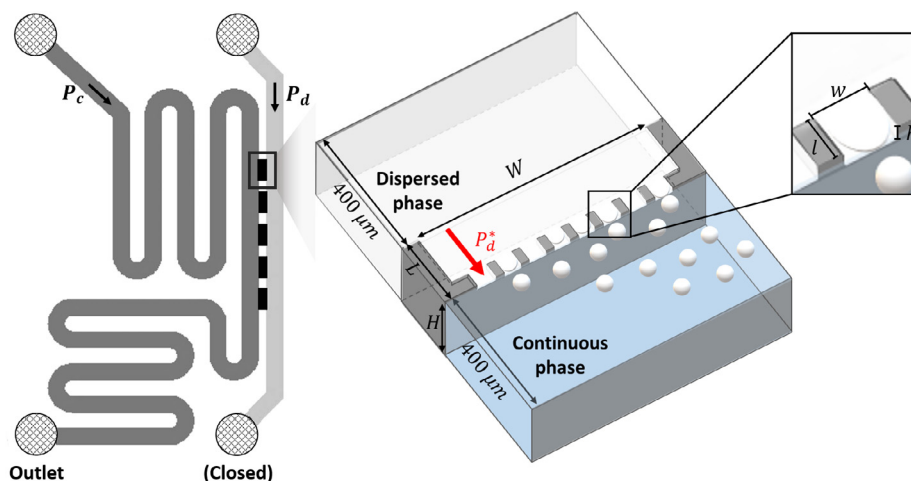


**Fig. 1.** Schematic illustration of the partitioned-EDGE microfluidic device: chip, plateau and pore. Chip (left): during the experiment the outlet of the dispersed phase channel is closed, and the air phase is forced to flow through the shallow plateau and pores under a pressure difference  $P_d^*$  (shown as red arrow). Plateau (middle) and pore (right): bubbles are formed from the pores' exit. White colour represents the air phase and blue colour represents the continuous phase. The characteristic dimensions are explained in the text; schematics are not drawn to scale. (For interpretation of the references to colour in this figure legend, the reader is referred to the web version of this article.)

and  $l, h, w$  the geometrical dimensions as mentioned above [38]. When this equation is used to calculate the hydrodynamic resistance of the shallow plateau, the geometrical dimensions used are  $W, L$  and  $h$ . The total hydrodynamic resistance of a single pore ( $\mathcal{R}_{pore}$ ) is approximated by the resistance of the pore given above plus that of the entry path in front of it: a section of the shallow plateau with width  $W/8$  and length  $L - l$ . This effective resistance is  $\mathcal{R}_{pore} \approx 7 \cdot 10^{14} \text{ kg/m}^4/\text{s}^2$ , and it has a significant contribution from the entry path on the plateau since that is relatively long. The considerable pore resistance enables complete filling of the entry plateau and thus ensures a high pressure stability of the pores against pressure fluctuations during the foaming process [21].

In our experiment, both the air and the continuous phases are pressure-driven, using a digital pressure controller ( $\pm 2 \text{ mbar}$ ) operated by Smart Interface Software (Elveflow<sup>®</sup>, France). To avoid invasion of the shallow plateau and the pores by the continuous phase before measurement we always first pressurize the air phase such that it continuously flows through the pores. Then, we pressurize the air and the continuous phases to values  $P_d$  and  $P_c$  above ambient  $P_0$ , respectively. It is important to realize that the pressure applied to the air phase,  $P_d$ , decays exclusively over the high-resistance shallow region; while the pressure applied to the continuous phase,  $P_c$ , decays approximately linearly over the collection channel (neglecting viscosity variations due to presence of bubbles), and reaches a value  $P_c/2$  at the location of the shallow plateau positioned half-way the channel. To understand bubble formation on a single-pore level, throughout our experiments we consider the pressure difference  $P_d^* = P_d - P_c/2$  which drives air flow through the shallow region, as shown in Fig. 1.

While studying the effect of  $P_d^*$ , we aim to keep the continuous phase velocity  $v_c$  constant to avoid effects related to shear differences. For practical purposes we need to operate within two distinct shear regimes with a transition at 1400 mbar. For  $P_d^* < 1400 \text{ mbar}$  we set the velocity at  $v_c = 0.20 \text{ m/s}$ . For  $P_d^* \geq 1400 \text{ mbar}$  we set the velocity at  $v_c = 1.03 \text{ m/s}$ . The higher velocity is needed to limit the extent of bubble crowding, which allows quantitative analysis of bubble formation up to  $P_d^* \sim 2000 \text{ mbar}$ . We have verified (ESI 5†) that this small variation in shear does not critically influence bubble behavior. In the high-pressure regime the flow rates of the two phases are interrelated, so we perform a series of calibration curves (ESI 1†) to set these velocity conditions. We further test  $P_d^*$  up to 2800 mbar using qualitative observations.

## 2.1. Image analysis

Bubble dynamics are observed using a microscope (Axiovert 200 MAT, Carl Zeiss B.V., the Netherlands) equipped with a high-speed camera (FASTCAM SA-Z, Photron Limited, Japan). For each experimental condition ( $P_d, P_c$ ), we record two in-line videos: one at a frame rate of 100,000 frames per second and with a resolution of  $0.973 \mu\text{m}$  per pixel for measuring bubble size; and the other one at 700,000 frames per second and with a resolution of  $0.973$  or  $0.402 \mu\text{m}$  per pixel for extracting formation dynamics of single bubbles such as the development of their diameter in time and the relevant time scales. We use a custom-written script in Matlab R2018b or Image J to extract average diameters of bubbles that are formed at the pores ( $d_0$ ; average of up to 30 bubbles) or through coalescence ( $d_{coal}$ ; average of up to 50 bubbles), after their size has stabilized (i.e. their size stays unchanged before they are flowing out of the field of view). They correspond to volumes denoted as  $V_0$  and  $V_{coal}$ , respectively. The size resolution is better than  $1 \mu\text{m}$ . The bubble size distribution is expressed by the coefficient of variation (CV), which is defined as  $CV(\%) = (\sigma/d) \times 100$  (in which  $\sigma$  is the standard deviation and  $d$  is the number-averaged bubble diameter). For the initial bubbles ( $d_0$ ), the CV provides a measurement, within an individual experiment, of the deviation of monodispersity that is expected under perfect conditions (identical pores and pressure differences, no flow interactions). In addition, we perform a duplicate experiment to demonstrate good reproducibility of  $d_0$  across experiments (ESI 2†). The first video also yields the formation frequency  $f_0$  of bubbles with diameter  $d_0$  and the effective formation frequency of coalesced, stabilized bubbles  $f_{coal} = f_0 V_0 / V_{coal}$ . Here,  $f_0$  is determined by counting formed bubbles within a set period of time. A duplicate results in ESI 2† shows the good reproducibility of  $f_0$  across experiments.

## 3. Results and discussions

### 3.1. Observations of bubble formation and coalescence

The pores start generating relatively small bubbles when the pressure difference  $P_d^*$  reaches 1100 mbar. With increasing  $P_d^*$  more and more bubbles are formed (see Fig. 2A, snapshots 1–2), until bubble formation suddenly becomes more chaotic, producing both small and large bubbles at around and above 1400 mbar (snap-

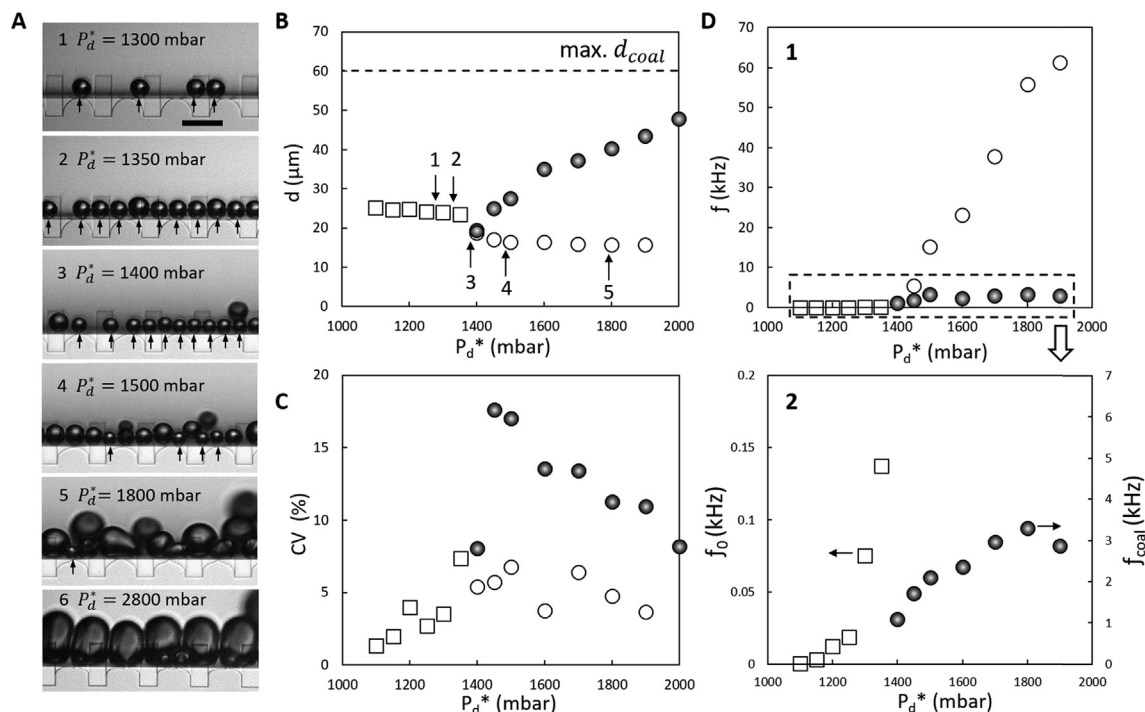


**Fig. 2.** Bubble observations as a function of  $P_d^*$ . A. Snapshots of bubble formation behavior. Arrows indicate the bubbles formed directly at the pores ( $d_0$ ). In snapshots 1–4, all bubbles have detached from the pores; while in snapshots 5–6 some bubbles are still connected via a neck to their corresponding meniscus. Scale bar is 50  $\mu\text{m}$ . B. Bubble diameters  $d_0$  and  $d_{coal}$ . Numbers refer to snapshots in A. At around 2400 mbar,  $d_{coal}$  converges to 60  $\mu\text{m}$  (dashed line). C. Coefficient of variation, which measures the span of the bubble size distribution shown in B. D. Bubble formation frequencies  $f_0$  and  $f_{coal}$ . The upper panel (D1) shows the full range up to 70 kHz, while the lower panel (D2) zooms in on the lower frequencies. Bubble frequencies are shown per pore. In B. – D. open symbols correspond to initial bubbles, and closed symbols correspond to coalesced, stabilized bubbles. The flow velocity  $v_c$  is indicated by symbols: 0.20 m/s (squares) at low  $P_d^*$  and 1.03 m/s (circles) at high  $P_d^*$ . Duplicate results for both bubble size and formation frequency show good reproducibility (ESI 2†).

shots 3–6). Visualization at high frame rate allows us to distinguish two different bubble formation mechanisms, which typically occur at similar time scales. Small bubbles (with an averaged diameter  $d_0$ ) snap off from the menisci in the pores; and larger equilibrated bubbles (with an averaged diameter  $d_{coal}$ ) are subsequently formed by coalescence in the collection channel – yet relatively close to the pore exits. Coalescence occurs primarily amongst successive bubbles from the same pore, while neighboring pores are spaced sufficiently to prevent neighboring bubble interactions.

In Fig. 2B and 2C we plot the bubble diameters  $d_0$  and  $d_{coal}$ , as well as the corresponding CV as a function of  $P_d^*$ . The bubble diameter  $d_0$  (open symbols) has two distinct, more or less constant, values in two distinct pressure regimes, which is similar to what has been found during emulsification performed in a similar device [21]. The diameter  $d_0$  is initially around 25  $\mu\text{m}$  and slightly decreases with increasing  $P_d^*$ . Monodispersity is high with a CV typically below 5%. The formation frequency  $f_0$  (see Fig. 2D) increases with  $P_d^*$ , yet remains relatively low, namely < 140 Hz. At around 1400 mbar, bubble formation changes drastically:  $d_0$  shows a step-wise decrease and then levels off at approximately 16  $\mu\text{m}$  when  $P_d^*$  is increased to up to 1900 mbar. This likely originates from both the stronger shear flow as well as the enhanced back-flow of the continuous phase, facilitating the neck shrinking process, as detailed in ESI 5†. The corresponding formation frequency  $f_0$  suddenly increases to kHz order and increases roughly linearly with  $P_d^*$ . The transition is accompanied by coalescence of bubbles, which has not been observed for droplets in the equivalent process of microfluidic emulsification, which is typically 100–1000 times slower. The stabilized, coalesced bubble diameter  $d_{coal}$  (closed symbols) increases with  $P_d^*$ . The CV of  $d_{coal}$  peaks at 1450 mbar since limited coalescence leads to a bi-disperse distribution of bubbles – yet it remains well below 20%,

and it decreases again when more bubbles coalesce at higher  $P_d^*$ . The coalescence phenomenon obviously reduces the effective formation frequency of stabilized bubbles to  $f_{coal}$ . This frequency increases for only a small range of  $P_d^*$  and then levels off at  $\sim 3$  kHz (see Fig. 2D2). We studied coalescence for an extended range of  $P_d^*$  up to 2800 mbar and found that  $d_{coal}$  levels off at around 60  $\mu\text{m}$  (with a CV typically around 10%) when  $P_d^*$  reaches 2400 mbar (dashed line in Fig. 2B). This diameter is identical to the pitch between pores, and indeed the coalesced bubbles are observed to be moved out of the range of newly formed bubbles as they are pushed away by their neighbors (ESI 3†), due to the so-called “squeezing” effect [23].

### 3.2. Dynamics of bubble formation at the pore

To understand the formation and coalescence behaviors outlined above, we focus on an individual pore and study the air flow in this pore, followed by expansion of a bubble into the continuous phase channel. Accordingly, a single bubble formation process is divided into two stages: the (pore) “filling” stage and the (bubble) “necking” stage. In Fig. 3, panel A shows the progression and shape of the meniscus in the two stages, while panel B includes the bubble formed during the necking stage. The stages of pore filling and bubble growth can be described using a quasi-static approach as the momentum of the gas is negligible compared to the static force of surface tension (see ESI 4†) [39]. The Laplace pressure over the air/water interface is calculated by  $\Delta P_L = \gamma \left( \frac{1}{R_1} + \frac{1}{R_2} \right)$ , with radii of curvature  $R_1$  and  $R_2$ . Fig. 3C shows three scenarios of the air/water interface during bubble formation, and at these locations the radii of curvature and thus the Laplace pressure are different. First, there is a two-dimensional meniscus in the pore ( $\Delta P_{L|pore}$ , 1: blue line).

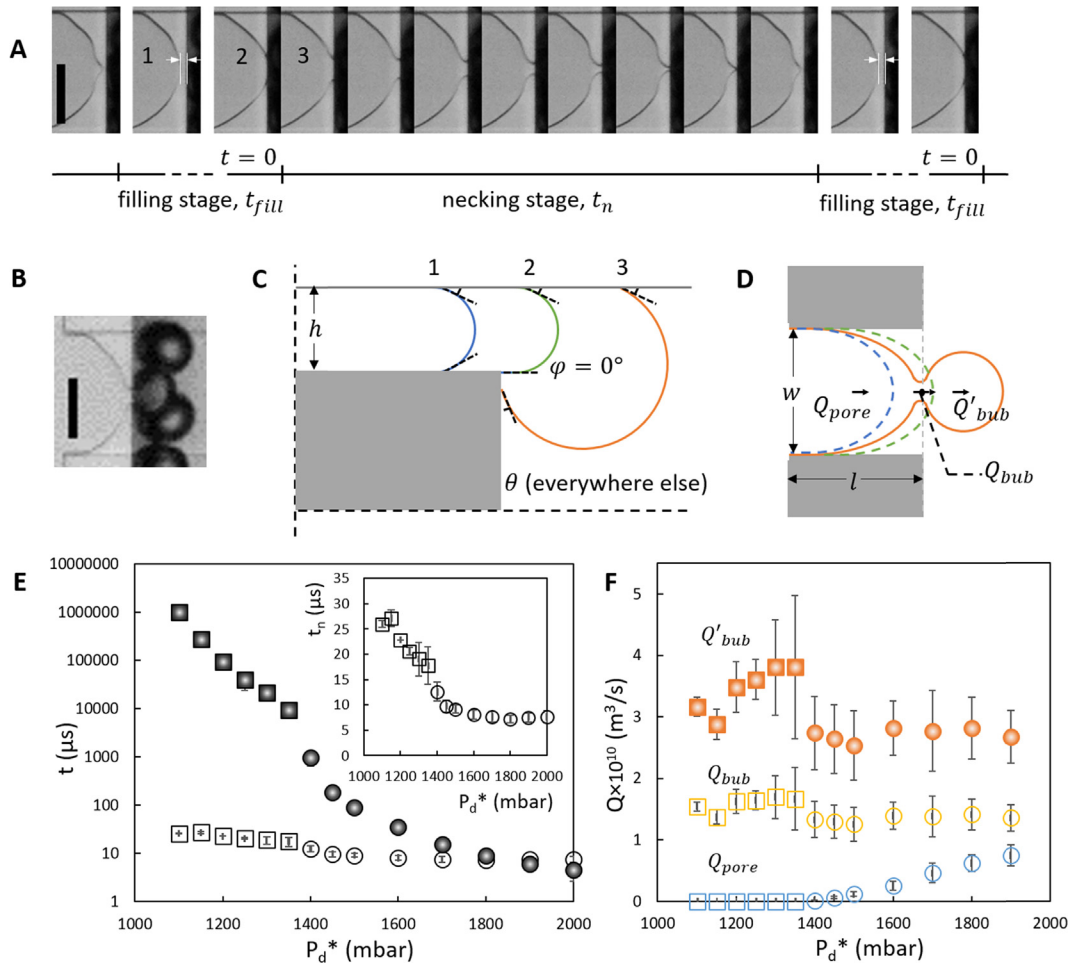


**Fig. 3.** Bubble dynamics at the pore. A. The meniscus behaviour during the filling and necking stages for  $P_d^* = 1400$  mbar. Necking stage:  $dt = 1.43 \mu\text{s}$  between frames; only two representative frames are shown for the (much longer) filling stage. The scale bar is  $20 \mu\text{m}$ . B. Snapshot of the necking process including growing bubble. The scale bar is  $20 \mu\text{m}$ . C. Schematic illustration (side view) of the shape of interface at three positions shown in A: 1 = meniscus inside the pore, 2 = meniscus pinning at the edge, 3 = expanding bubble (three-dimensional).  $\theta$  is the contact angle between the meniscus and the pore walls;  $\varphi$  is the pinned angle. D. Schematic illustration (top view) of the air flow rates. E. Log-scale plot of the filling time ( $t_{fill}$ , closed symbols) and the necking time ( $t_n$ , open symbols) as a function of  $P_d^*$ . Inset:  $t_n$  on linear scale. The filling time is observed and averaged over multiple pores; for  $P_d^* < 1400$  mbar the filling time is simply estimated by  $1/f_0$ , ignoring the negligible contribution of  $t_n$ . F. Air flow rates  $Q'_{bub}$  (orange, closed symbols),  $Q_{bub}$  (yellow, open symbols) and  $Q_{pore}$  (blue, open symbols) as a function of  $P_d^*$ . In E,F, error bars (included for all data points) are not visible when they are smaller than the symbol. Different symbols represent different flow velocities:  $v_c = 0.20$  m/s (squares) and  $1.03$  m/s (circles). (For interpretation of the references to colour in this figure legend, the reader is referred to the web version of this article.)

When the meniscus advances in the shallow pore, entering the pore filling stage,  $\Delta P_L|_{pore} \approx 2\gamma\cos(\theta)/h$  with contact angle  $\theta$  and the radius of curvature  $h/(2\cos(\theta))$  since  $h \ll w$ . Second, the meniscus is pinned at the pore edge ( $\Delta P_L|_{pore,max}$ , 2: green line). This causes air to collect at the edge of the pore and the meniscus reaches its maximum Laplace pressure  $\Delta P_L|_{pore,max} \approx \gamma[1 + \cos(\theta)]/h$ , with the contact angle between the meniscus and the bottom wall of the pore being zero [18]. Note that  $\Delta P_L|_{pore,max}$  is only marginally larger than  $\Delta P_L|_{pore}$  for small contact angle  $\theta$ , which is the case here as the glass walls are wetted by the aqueous phase. Finally, the meniscus leaps over the edge and a three-dimensional bubble is forming in the continuous phase channel ( $\Delta P_L|_{bub}$ , 3: orange line), entering the necking stage. Over time the bubble diameter  $d(t)$  increases and leads to a steep decrease of Laplace pressure towards  $\Delta P_L|_{bub} \approx 4\gamma/d_0$ , which induces a pressure jump in the continuous phase driving its backflow from the continuous phase channel towards the narrow air thread or neck at the end of the pore [40]. During the necking stage, bubble growth and contraction of the neck happen simultaneously until the neck width narrows to the order of the pore's height [22]. Owing to the shallow pore height, the neck will then

collapse extremely fast and generate a bubble. At the same time, the meniscus relaxes and retracts back into the pore for a finite distance. Subsequently, the next filling stage starts to replenish the detached volume of air (last two snapshots in Fig. 3A).

The time scales for both stages are defined as the filling time  $t_{fill}$  and the necking time  $t_n$  (Fig. 3A). The full time scale for one bubble formation is then  $\tau = t_{fill} + t_n$ . The filling time  $t_{fill}$  is infinitely long at low pressures, which corresponds to absence of bubble formation. We can detect the first bubbles at 1100 mbar, when bubbles are formed at finite intervals of 1 s (which is the detection limit in our recordings). When  $P_d^*$  is increased to 1400 mbar, the filling time steeply decreases over several orders of magnitude to  $\sim 1$  ms (closed symbols in Fig. 3E). It keeps decreasing towards approximately  $5 \mu\text{s}$  when  $P_d^*$  is increased to up to 2000 mbar. The necking time  $t_n$  also shows a decreasing trend, yet it is less steep:  $t_n$  first decreases from  $25 \mu\text{s}$  to  $14 \mu\text{s}$  when  $P_d^*$  is increased to 1400 mbar and slowly converges to  $\sim 7 \mu\text{s}$  (open symbols in Fig. 3E) at 1600 mbar, and then it remains constant. From 1900 mbar onwards the filling time  $t_{fill}$  is shorter than the necking time  $t_n$ . When  $t_{fill}$  is much shorter than  $t_n$ , this occasionally results in the formation of two necks from one pore as mentioned in ESI 3†.

To understand the mechanism of bubble formation, we use the quasi-static approach to quantify and compare the flow rates of air through the pore, and into the bubble. It has also been argued that the surfactant coverage on an expanding droplet is homogenous [41], which allows to ignore Marangoni effects during its growth (up to the final snap-off process). During the filling stage, the flow of air through the pore is driven by the pressure difference  $P_d^* - \Delta P_{L|pore}$ . Since this pressure difference is at maximum 10% of the background pressure  $P_c/2 + P_0$ , compressibility effects can be neglected and the pore flow rate can be simply described by the Hagen-Poiseuille law:  $Q_{pore} = (P_d^* - \Delta P_{L|pore})/\mathcal{R}_{pore}$ , with  $\mathcal{R}_{pore}$  the hydrodynamic resistance of the pore defined above. During the necking stage, two flows can be identified: pore flow and flow from the developing neck into the bubble. The pore flow rate is assumed to remain constant at  $Q_{pore}$  since both  $P_d^*$  and the Laplace pressure of the meniscus constricted within the pore ( $\Delta P_{L|pore} \sim 1/h$ ) remain unchanged. The flow into the bubble follows a steep Laplace pressure gradient  $\Delta P_{L|pore} - \Delta P_{L|bub}$ , accompanied by air expansion due to compressibility. Thus, we define two flow rates towards the bubble:  $Q_{bub}$  is the flow rate at the location and local pressure of the neck, and  $Q'_{bub}$  is the (increased) flow rate into the growing bubble (Fig. 3D). A bubble will be formed if the flow rate out of the neck region is higher than the flow rate into it:  $Q_{bub} > Q_{pore}$  [26].

We analyse these flow rates starting from  $Q'_{bub}$  that can be measured directly from the growth rate of bubbles. Experiments at low  $P_d^*$  demonstrate that bubble volume increases linearly in time with a constant inflow  $Q'_{bub}$  until snap-off (ESI 6†). The bubble has a single growth phase, since the shallowness of the pore strongly limits volume addition from (i) the air ridge pinned at the edge of the pore (Fig. 3C line 2) and (ii) the extremely fast break-up stage (ESI 7†). The growing bubble quickly reaches a curvature that is negligible compared to the pore's height, and thus the bubble volume increases linearly, driven by a constant Laplace pressure  $\Delta P_{L|pore}$  [20]. We can thus obtain  $Q'_{bub}$  from the ratio  $V_0/t_n$ , which is shown in Fig. 3F (orange, closed symbols) for our full range of pressure differences  $P_d^*$ .  $Q'_{bub}$  has a constant value at high pressure differences, showing that the driving pressure  $\Delta P_{L|pore}$  is independent of  $P_d^*$ . At low pressure differences,  $Q'_{bub}$  is an increasing function of  $P_d^*$ , which is due to air expansion along the steep pressure gradient. We calculate the flow rate in the neck itself using the ideal gas law (ESI 8†), to remove the effect of air expansion:  $Q_{bub} = Q'_{bub} \frac{[P_c/2+P_0]}{[\Delta P_{L|pore}+P_c/2+P_0]}$ . Indeed, Fig. 3F shows that  $Q_{bub}$  (yellow, open symbols) is constant not only for high, but also for low  $P_d^*$ . This separation into two distinct regimes will be addressed in the section below.

The pore flow rate  $Q_{pore}$  cannot be extracted directly from recorded videos, but we can calculate it from mass conservation throughout one bubble formation period. At the local (fixed) pressure of the neck we have  $Q_{pore}\tau = Q_{bub}t_n$ . Fig. 3F shows the  $Q_{pore}$  values (blue, open symbols) derived based on the above-determined  $Q_{bub}$ , as well as time scales  $t_n$  and  $\tau$  (see Fig. 3E).  $Q_{pore}$  increases with  $P_d^*$ , although it is nearly zero for pressure differences below 1400 mbar – in line with the steeply increasing filling time (Fig. 3E), and again confirming the existence of two bubble formation regimes. We indeed find  $Q_{bub} > Q_{pore}$  for all pressure differences up to 2000 mbar, confirming the criterion for bubble formation to take place. At even higher  $P_d^*$  (above 2400 mbar), the behaviour changes, namely, we observe the formation of two neighboring (and merging) necks from a single pore (ESI 3†). This is in contrast to the catastrophic 'blow-up' behavior demonstrated (for droplets) [12,16,22], which would involve the abrupt transi-

tion towards a continuous thread of air (or liquid) flowing out of the pore.

### 3.3. Two bubble formation regimes: the role of the dynamic adsorption

One question about bubble formation still remains: why do the pore flow rate (Fig. 3F) and thus the bubble formation frequency (Fig. 2D) decrease dramatically at pressure differences below 1400 mbar? The observed transition in bubble behavior coincides with the pore Laplace pressure  $\Delta P_{L|pore} \approx 2\gamma\cos(\theta)/h \approx 1400 \pm 50$  mbar obtained for an air/water interface free of proteins (with  $\gamma_0$  assumed to be 72.4 mN/m) and a low water contact angle on the hydrophilic glass surface ( $\theta \approx 15^\circ$ ). Hence, for  $P_d^* \geq 1400$  mbar, the pressure difference driving pore flow,  $P_d^* - \Delta P_{L|pore}$ , is positive at all times. This leads to immediate air flow and short bubble formation time ( $\tau$ ) of approximately 10 – 1000 microseconds (Fig. 3E). We call this the "steady" regime: as a result of the fast pore dynamics, adsorption of whey proteins to the meniscus can be neglected and  $\Delta P_{L|pore}$  is virtually constant irrespective of applied pressure difference, namely 1400 mbar. Thus, on one hand,  $Q'_{bub}$  has a fixed value independent of  $P_d^*$  as the driving pressure for air flow into the bubble is constant; on the other hand,  $Q_{pore}$  increases linearly with  $P_d^* - \Delta P_{L|pore}$ . Both are in line with our results shown in Fig. 3F. The latter also allows us to extract the hydrodynamic resistance of the pore  $\mathcal{R}_{pore} = 6 \cdot 10^{14}$  kg/m<sup>4</sup>/s<sup>2</sup>, which is in close agreement with the geometry-based estimation that we made earlier. The small deviation might be due to the fabrication accuracy of the geometry (e.g. with  $h$  being slightly larger than 1  $\mu$ m). Finally, the constant bubble diameter  $d_0$  in this steady regime (16  $\mu$ m, see Fig. 2B) is a result of constant  $Q'_{bub}$  and necking time. This decouples the bubble volume from the bubble frequency that can be tuned by varying  $P_d^*$ .

For  $P_d^* < 1400$  mbar, pore filling and the subsequent necking process are inhibited when no protein adsorption takes place. Indeed, when we gradually decrease  $P_d^*$  an abrupt transition is observed at 1390 mbar when pure water is used as the continuous phase (Fig. 4 inset 2). The air/water interface retracts from the pores and the shallow plateau (see Fig. 4 insets 1,2). However, when whey proteins are present in the continuous phase, bubble formation is initialized at a much lower pressure of  $P_d^* = 1100$  mbar. Even though we cannot directly measure the (dynamic) surface tension of the meniscus, proteins must adsorb in order to gradually lower the surface tension and thus the pore Laplace pressure  $\Delta P_{L|pore}$ . This induces a lag period in the filling time, required for  $\Delta P_{L|pore}$  to decrease below  $P_d^*$  [42]. Subsequently, the air phase starts flowing towards the edge of the pore, driven by a near-zero pressure difference; and eventually a bubble starts forming at the edge. The observed filling time thus strongly diverges with decreasing  $P_d^*$ , which is in agreement with Fig. 3E; and at the same time, the calculated pore flow rate vanishes (Fig. 3F). We call this the "dynamic" regime. A similar steep decrease in bubble formation frequency with decreasing  $P_d^*$  is observed for experiments with varying protein concentrations (see Fig. 4). These protein solutions of 1 – 10% wt. have very similar quasi-equilibrium surface tension of  $\sim 49$  mN/m (measured by pendant drop tensiometry). However, a higher protein concentration allows for faster protein adsorption, so the bubble formation frequency is expected to increase with protein concentration – as can be confirmed in Fig. 4. The apparent decrease of initialization pressure with increasing protein concentration is a detection artifact since we are only able to detect the occurrence of bubbles down to a frequency of 1 bubble per second. In fact, based on a surface tension of 49 mN/m, the initialization pressure would be approximately 950 mbar, which is consistent

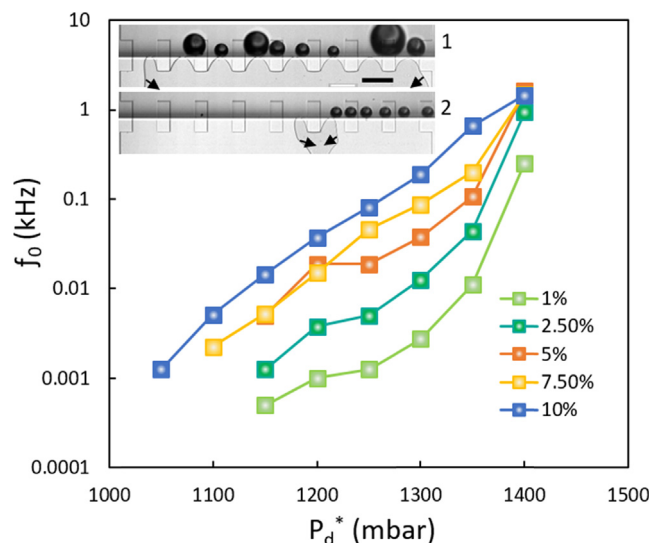


**Fig. 4.** Dynamic adsorption effects. Bubble formation frequency as a function of  $P_d^*$  (up to 1400 mbar) for a range of protein concentrations. Here, protein solutions have been adjusted to a constant viscosity of 2 mPa·s using glycerol, which has negligible effect on surface tension (<2 mN/m for a maximum of 20% wt. glycerol). Duplicate experimental results for 10% wt. whey protein solution (as an example) show good overlap (ESI 2†). Inset: bubble formation in absence of proteins. The markers 1 – 2 represent: 1 – at 1400 mbar and 2 – 1390 mbar, respectively, with pure water. The arrows indicate the retracting behaviour of the meniscus. (Note that bubbles will extensively coalesce due to the absence of proteins.) The scale bar is 50  $\mu$ m.

with our measurements and with the possible pinning effects at very low pressure differences.

Irrespective of the extremely slow pore flow rate in the dynamic regime, the air flow into the bubble remains surprisingly fast since its driving pressure is  $\Delta P_L|_{pore}$ , which is just a few hundred mbar below the steady-regime value of 1400 mbar. Fig. 3F shows that  $Q_{bub}$  is actually a bit higher before the transition at 1400 mbar, which may be explained by a change in the hydrodynamic resistance of the neck, which has different geometry in the two distinct regimes (ESI 5†). Moreover, the minor differences in bubble growth

rate across experimental conditions reinforces the idea that Marangoni flows have no significant effect on bubble expansion. On the other hand, the final thinning of the neck may locally cause heterogeneity of surface coverage and thus Marangoni flows that dictate necking time [43]. In our experiments, we observe that the combined effect of decreasing necking time and increasing  $Q'_{bub}$  yields a more-or-less constant bubble diameter  $d_0$  in the dynamic regime (25  $\mu$ m, see Fig. 2B).

### 3.4. Bubble coalescence near the pore

The transition between the dynamic and steady regimes has direct implications for the coalescence stability of bubbles formed at the pores. Proteins may adsorb to the meniscus in the pore, and to the bubble interface, either during its expansion or afterwards in the collection channel. Since the bubble interface expands significantly it is assumed that proteins previously adsorbed to the meniscus during the filling stage play only a minor role in terms of surface coverage. The amount of adsorption during bubble expansion is expected to be limited and to be very similar across all experimental conditions since both the expansion time (necking time in Fig. 3E) and bubble growth rate  $Q'_{bub}$  (Fig. 3F) show only small variations. Across the experimental conditions, only for  $P_d^* < 1400$  mbar bubbles are immediately stable against coalescence, while for  $P_d^* \geq 1400$  mbar, bubbles coalesce to an extent that is strongly dependent on the bubble formation time  $\tau$ . This demonstrates the intersection of time scales of bubble formation and protein adsorption, with a crucial time scale of 1 ms (see Fig. 5). For  $\tau > 1$  ms (here obtained when  $P_d^* < 1400$  mbar), the bubble interface can be stabilized with proteins, after this bubble has been released from the pore, well before the next bubble collides. On the other hand, for  $P_d^* \geq 1400$  mbar, successive bubbles are formed within short time scales down to tens of microseconds. Even if proteins may adsorb to the bubble surface, the partial surface coverage is not sufficient at the time of interaction with successive bubbles. As a result, the bubbles coalesce, showing an increasing number of coalescence events  $N = (V_{coal}/V_0) - 1$  as a function of increasing  $P_d^*$  when  $\tau$  decreases below 1 ms (see Fig. 5). Eventually, the successive coalescence of bubbles stops when the growing bubble

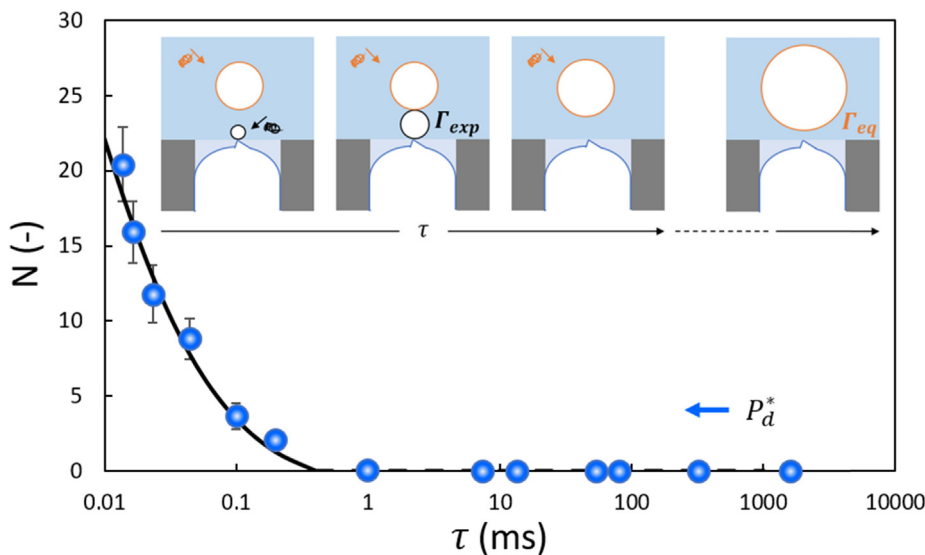


**Fig. 5.** Bubble coalescence. Number ( $N = k - 1$ ) of coalescence events as a function of bubble formation time ( $\tau$ ). From right to left,  $\tau$  corresponds to  $P_d^*$  ranging from 1100 to 1900 mbar (indicated by an arrow). Inset: Schematics of protein adsorption during one bubble formation/ coalescence cycle (the first three snapshots) and the end of a coalescence series. Protein adsorption to the interface of the expanding bubble and the coalesced, waiting bubble is indicated by black and orange arrows, respectively. Blue symbols: experimental data. Solid line: fit of our semi-empirical coalescence model (ESI 9†) to the data. Dashed line: regime of non-coalescence for  $\tau > t_1$ . (For interpretation of the references to colour in this figure legend, the reader is referred to the web version of this article.)

reaches stability, which is assumed to happen at near-monolayer surface coverage [44,45].

We have captured this conceptual understanding in a semi-empirical coalescence model (ESI 9†). It takes into account protein accumulation at the interface of both the expanding bubble (reaching coverage  $\Gamma_{exp}$  upon snap-off from the pore) and the growing bubble in the collection channel. This happens in a series of subsequent coalescence cycles, in which the newly formed bubble merges into the waiting, growing, bubble. The process ends when the surface coverage needed for stabilization,  $\Gamma_{eq}$ , is obtained. The protein mass balance is derived in ESI 9† and is formulated by  $k^{2/3} = k \frac{\Gamma_{exp}}{\Gamma_{eq}} + \left(1 - \frac{\Gamma_{exp}}{\Gamma_{eq}}\right) \left(\frac{t_k}{t_1}\right) \left[\sum_{i=1}^{k-1} i^{2/3} + \frac{k^{2/3}}{2}\right]$ . The number of bubbles that coalesce ( $k$ ) is described by three parameters, namely the independent variable  $t_k$  and the two fit parameters that are  $\Gamma_{exp}/\Gamma_{eq}$  and  $t_1$ .  $t_k$  is the time of a single coalescence cycle which is equivalent to the experimental bubble formation time  $\tau$ ; and  $t_1$  is the minimum bubble formation time required to immediately stabilize a bubble and thus to prevent any coalescence. Fitting the model to the experimental data yields  $\Gamma_{exp}/\Gamma_{eq} = 0.26 \pm 0.03$  and  $t_1 = 0.40 \pm 0.07$  ms. Our simple model captures the data well, and yields a realistic stabilization time which is close to the time scale required for bubble stabilization in the steady regime ( $\sim 1$  ms). The model provides a framework for future refinement, in particular the substitution of a rate equation for protein adsorption; and the dependency of stabilization time on process conditions such as protein concentration and continuous phase viscosity. The latter are potential routes to control bubble coalescence, and will be discussed in detail in future work.

#### 4. Conclusions

Time scales for surfactant transport dynamics and adsorption are influenced by a variety of aspects such as the bulk concentration and diffusivity of the surfactant, curvature of the interface and presence of bulk convection [37]. As a result, it is nearly impossible to relate macroscopic interfacial tension measurements (performed in pendant drop tensiometer) to the stabilization of bubbles and droplets formed at the microscale. Even though both observations are an effect of surfactant adsorption, the transport dynamics are vastly different, from diffusion-dominated conditions for the first, to much more dynamic conditions for the latter. Microfluidic techniques have tackled some of these issues, namely by measuring interfacial tension (for example, through deformation of droplets in contraction–expansion channels [46,47], droplet size resulting from well-defined shear conditions [34,48], or capillary–pressure based microtensiometry [49,50]) or studying coalescence upon droplet–droplet interactions [35,51–54] both at the microscale. However, these approaches still have limited time resolution and range. Three key characteristics of the partitioned-EDGE device used here are that we can *directly* study coalescence; we study it *immediately after* the formation of a fresh bubble interface; and that we can vary bubble formation time ( $\tau$ ) over five orders of magnitude, while keeping other aspects of the formation dynamics roughly constant (such as bubble size, bubble expansion rate and flow conditions in the collection channel). Our shortest bubble formation time is  $\sim 10$   $\mu$ s, which is significantly faster than other recent studies [18,22,28], and the longest bubble formation time is at a second time scale.

We demonstrate a rich bubble behavior with co-existence of bubble formation and coalescence at similar time scales. This is extremely relevant for large-scale foaming operations and is not incorporated in more traditional microfluidic studies that often exclude coalescence when studying the mechanism of bubble formation [9,15,18,22,28,55]. Distinct foaming regimes appear depending on the time scales of bubble formation and surfactant

adsorption. At low  $P_d^*$ , protein adsorption gradually lowers the surface tension and thus initiates bubble formation after a lag time ( $\gg 1$  ms). The resulting bubble formation frequency is relatively low, yet coalescence is prevented by timely creation of a stabilizing protein layer. At high  $P_d^*$ , bubble formation does not suffer from this adsorption lag. The resulting formation frequency is high, and bubbles show finite coalescence as they interact before they are fully stabilized. The shortest formation time at which bubbles are still stable is between 0.2 and 1 ms, which can be determined with very high precision in this partitioned-EDGE device, and is in line with the value predicted by our empirical coalescence model. The stabilization time gives an estimate for the time scale of protein adsorption, which is governed by the enhanced mass transfer due to bulk convection and high protein concentration. Protein adsorption to the expanding bubble interface (in a time scale  $< 25$   $\mu$ s) will be limited, thus having limited effect on the growth dynamics (growth rate and shape) of the bubbles. Our next step is to further develop the current system as an analytic tool to quantify and predict bubble coalescence *via* device geometry, fluid and protein properties and operation conditions.

#### CRedit authorship contribution statement

**Boxin Deng:** Conceptualization, Methodology, Investigation, Formal analysis, Visualization, Writing - original draft. **Karin Schroën:** Methodology, Supervision, Writing - review & editing. **Joliet Ruyter:** Methodology, Conceptualization, Supervision, Writing - original draft.

#### Declaration of Competing Interest

The authors declare that they have no known competing financial interests or personal relationships that could have appeared to influence the work reported in this paper.

#### Acknowledgement

The authors would like to thank the China Scholarship Council (grant number 201806790006) and FrieslandCampina for financial support.

#### Appendix A. Supplementary data

Supplementary data to this article can be found online at <https://doi.org/10.1016/j.jcis.2021.06.014>.

#### References

- [1] P. Garstecki, I. Gitlin, W. Diluzio, G.M. Whitesides, E. Kumacheva, H.A. Stone, Formation of monodisperse bubbles in a microfluidic flow-focusing device, *Appl. Phys. Lett.* 85 (2004) 2649–2651, <https://doi.org/10.1063/1.1796526>.
- [2] P. Garstecki, H.A. Stone, G.M. Whitesides, Mechanism for flow-rate controlled breakup in confined geometries: A route to monodisperse emulsions, *Physical Review Lett.* 94 (2005), <https://doi.org/10.1103/PhysRevLett.94.164501> 164501.
- [3] E. Lorenceau, Y.Y.C. Sang, R. Höhler, S. Cohen-Addad, A high rate flow-focusing foam generator, *Physics of Fluids* 18 (2006), <https://doi.org/10.1063/1.2353799> 097103.
- [4] M.T. Sullivan, H.A. Stone, The role of feedback in microfluidic flow-focusing devices, *Philos. Trans. R. Soc. A Math. Phys. Eng. Sci.* 366 (2008) 2131–2143, <https://doi.org/10.1098/rsta.2008.0003>.
- [5] P. Garstecki, M.J. Fuerstman, H.A. Stone, G.M. Whitesides, Formation of droplets and bubbles in a microfluidic T-junction - Scaling and mechanism of break-up, *Lab on a Chip* 6 (2006) 437–446, <https://doi.org/10.1039/b510841a>.
- [6] J.H. Xu, S.W. Li, G.G. Chen, G.S. Luo, Formation of Monodisperse Microbubbles in a Microfluidic Device, *AIChE J.* 52 (2006) 2254–2259, <https://doi.org/10.1002/aic.10824>.
- [7] K. Wang, Y.C. Lu, J.H. Xu, J. Tan, G.S. Luo, Generation of Micromonodispersed Droplets and Bubbles in the Capillary Embedded T-junction Microfluidic Devices, *AIChE J.* 57 (2011) 299–306, <https://doi.org/10.1002/aic>.

- [8] J.H. Xu, S.W. Li, J. Tan, Y.J. Wang, G.S. Luo, Preparation of Highly Monodisperse Droplet in a T-Junction Microfluidic Device, *AIChE J.* 52 (2006) 3005–3010, <https://doi.org/10.1002/aic>.
- [9] M. Hashimoto, S.S. Shevkoplyas, B. Zasońska, T. Szymborski, P. Garstecki, G.M. Whitesides, Formation of bubbles and droplets in parallel, coupled flow-focusing geometries, *Small* (Weinheim an der Bergstrasse, Germany) 4 (2008) 1795–1805, <https://doi.org/10.1002/sml.200800591>.
- [10] T. Kawakatsu, Y. Kikuchi, M. Nakajima, Regular-Sized Cell Creation in Microchannel Emulsification by Visual Microprocessing Method, *Journal of the American Oil Chemists Society* 74 (1997) 317–321, <https://doi.org/10.1252/jcej.32.241>.
- [11] S. Sugiura, M. Nakajima, S. Iwamoto, M. Seki, Interfacial tension driven monodisperse droplet formation from microfabricated channel array, *Langmuir* 17 (2001) 5562–5566, <https://doi.org/10.1021/la010342y>.
- [12] N. Mittal, C. Cohen, J. Bibette, N. Bremond, Dynamics of step-emulsification: From a single to a collection of emulsion droplet generators, *Physics of Fluids* 26 (2014), <https://doi.org/10.1063/1.4892949> 082109.
- [13] I. Kobayashi, T. Takano, R. Maeda, Y. Wada, K. Uemura, M. Nakajima, Straight-through microchannel devices for generating monodisperse emulsion droplets several microns in size, *Microfluid. Nanofluidics*. 4 (2008) 167–177, <https://doi.org/10.1007/s10404-007-0167-2>.
- [14] K.C. Van Dijke, G. Veldhuis, K. Schroën, R.M. Boom, K. Schroën, R.M. Boom, Simultaneous Formation of Many Droplets in a Single Microfluidic Droplet Formation Unit, *AIChE J.* 56 (2010) 833–836, <https://doi.org/10.1002/aic>.
- [15] M. Yasuno, S. Sugiura, S. Iwamoto, M. Nakajima, A. Shono, K. Satoh, Monodisperse microbubble formation using microchannel technique, *AIChE J.* 50 (2004) 3227–3233, <https://doi.org/10.1002/aic.10276>.
- [16] S. Sugiura, M. Nakajima, N. Kumazawa, S. Iwamoto, M. Seki, Characterization of spontaneous transformation-based droplet formation during microchannel emulsification, *Journal of Physical Chemistry B* 106 (2002) 9405–9409, <https://doi.org/10.1021/jp0259871>.
- [17] K.C. Van Dijke, K.C.P.G.H. Schroën, R.M. Boom, Microchannel emulsification: From computational fluid dynamics to predictive analytical model, *Langmuir* 24 (2008) 10107–10115, <https://doi.org/10.1021/la801411x>.
- [18] M. Stoffel, S. Wahl, E. Lorenceau, R. Höhler, B. Mercier, D.E. Angelescu, Bubble production mechanism in a microfluidic foam generator, *Physical Review Lett.* 108 (2012), <https://doi.org/10.1103/PhysRevLett.108.198302> 198302.
- [19] Z. Zhang, S. Jiang, C. Zhu, Y. Ma, T. Fu, Bubble formation in a step-emulsification microdevice with parallel microchannels, *Chemical Engineering Science* 224 (2020), <https://doi.org/10.1016/j.ces.2020.115815> 115815.
- [20] E. Amstad, M. Chemama, M. Eggersdorfer, L.R. Arriaga, M.P. Brenner, D.A. Weitz, Robust scalable high throughput production of monodisperse drops, *Lab on a Chip* 16 (2016) 4163–4172, <https://doi.org/10.1039/c6lc01075j>.
- [21] S. Sahin, K. Schroën, Partitioned EDGE devices for high throughput production of monodisperse emulsion droplets with two distinct sizes, *Lab on a Chip* 15 (2015) 2486–2495, <https://doi.org/10.1039/c5lc00379b>.
- [22] E. Crestel, L. Derzsi, H. Bartolomei, J. Bibette, N. Bremond, Emulsification with rectangular tubes, *Physical Review Fluids* 4 (2019), <https://doi.org/10.1103/physrevfluids.4.073602> 073602.
- [23] S. ten Klooster, S. Sahin, K. Schroën, Monodisperse droplet formation by spontaneous and interaction based mechanisms in partitioned EDGE microfluidic device, *Scientific Reports* 9 (2019) 7820, <https://doi.org/10.1038/s41598-019-44239-7>.
- [24] K. Van Dijke, R. De Ruiter, K. Schroën, R. Boom, The mechanism of droplet formation in microfluidic EDGE systems, *Soft Matter* 6 (2010) 321–330, <https://doi.org/10.1039/b916141d>.
- [25] K. Van Dijke, I. Kobayashi, K. Schroën, K. Uemura, M. Nakajima, R. Boom, Effect of viscosities of dispersed and continuous phases in microchannel oil-in-water emulsification, *Microfluid. Nanofluidics*. 9 (2010) 77–85, <https://doi.org/10.1007/s10404-009-0521-7>.
- [26] M.L. Eggersdorfer, H. Seybold, A. Ofner, D.A. Weitz, A.R. Studart, Wetting controls of droplet formation in step emulsification, *PNAS* 115 (2018) 9479–9484, <https://doi.org/10.1073/pnas.1803644115>.
- [27] A. Montessori, M. Lauricella, S. Succi, E. Stolovicki, D. Weitz, Elucidating the mechanism of step emulsification, *Physical Review Fluids* 7 (2018), <https://doi.org/10.1103/PhysRevFluids.3.072202> 072202.
- [28] S. Mi, T. Fu, C. Zhu, S. Jiang, Y. Ma, Mechanism of bubble formation in step-emulsification devices, *AIChE J.* 66 (2019) 16777, <https://doi.org/10.1002/aic.16777>.
- [29] G. Narsimhan, N. Xiang, Role of Proteins on Formation, Drainage, and Stability of Liquid Food Foams, *Annu. Rev. Food Sci. Technol.* 9 (2018) 45–63, <https://doi.org/10.1146/annurev-food-030216-030009>.
- [30] K.C. van Dijke, K. Schroën, A. van der Padt, R. Boom, EDGE emulsification for food-grade dispersions, *Journal of Food Engineering* 97 (2010) 348–354, <https://doi.org/10.1016/j.jfoodeng.2009.10.028>.
- [31] S.M. Jafari, E. Assadpoor, Y. He, B. Bhandari, Re-coalescence of emulsion droplets during high-energy emulsification, *Food Hydrocoll.* 22 (2008) 1191–1202, <https://doi.org/10.1016/j.foodhyd.2007.09.006>.
- [32] K. Muijlwijk, Microfluidic methods to study emulsion formation, Wageningen University & Research (2017), <https://doi.org/10.18174/403476>.
- [33] C. Güell, M. Ferrando, A. Trentin, K. Schroën, Apparent interfacial tension effects in protein stabilized emulsions prepared with microstructured systems, *Membranes* (Basel). 7 (2017) 1–12, <https://doi.org/10.3390/membranes7020019>.
- [34] K. Muijlwijk, E. Hinderink, D. Ershov, C. Berton-Carabin, K. Schroën, Interfacial tension measured at high expansion rates and within milliseconds using microfluidics, *Journal of Colloid and Interface Science* 470 (2016) 71–79, <https://doi.org/10.1016/j.jcis.2016.02.041>.
- [35] K. Muijlwijk, I. Colijn, H. Harsono, T. Krebs, C. Berton-Carabin, Coalescence of protein-stabilised emulsions studied with microfluidic, *Food Hydrocoll.* 70 (2017) 94–104, <https://doi.org/10.1016/j.foodhyd.2017.03.031>.
- [36] E.B.A. Hinderink, J. De Ruiter, J. De Leeuw, K. Schro, M. Leonard, C. Sagis, C.C. Berton-carabin, Early film formation in protein-stabilised emulsions : Insights from a microfluidic approach, *Food Hydrocoll.* 118 (2021), <https://doi.org/10.1016/j.foodhyd.2021.106785>.
- [37] Y. Chen, S. Narayan, C.S. Dutcher, Phase-Dependent Surfactant Transport on the Microscale: Interfacial Tension and Droplet Coalescence, *Langmuir* 36 (2020) 14904–14923, <https://doi.org/10.1021/acs.langmuir.0c02476>.
- [38] H. Bruus, *Theoretical microfluidics*, Oxford University Press Inc., New York, 2008, <https://doi.org/10.5860/choice.45-5602>.
- [39] W. Drenckhan, A. Saint-Jalmes, The science of foaming, *Advances in Colloid and Interface Science* 222 (2015) 228–259, <https://doi.org/10.1016/j.cis.2015.04.001>.
- [40] R. Dangla, E. Fradet, Y. Lopez, C.N. Baroud, The physical mechanisms of step emulsification, *Journal of Physics: D: Applied Physics* 46 (2013), <https://doi.org/10.1088/0022-3727/46/11/114003> 114003.
- [41] J.H. Xu, P.F. Dong, H. Zhao, C.P. Tostado, G.S. Luo, The dynamic effects of surfactants on droplet formation in coaxial microfluidic devices, *Langmuir* 28 (2012) 9250–9258, <https://doi.org/10.1021/la301363d>.
- [42] M.J. Geerken, R.G.H. Lammertink, M. Wessling, Interfacial aspects of water drop formation at micro-engineered orifices, *Journal of Colloid and Interface Science* 312 (2007) 460–469, <https://doi.org/10.1016/j.jcis.2007.03.074>.
- [43] A. Shelley L., Droplets and Bubbles in Microfluidic Devices, *Annu. Rev. Fluid Mech.* 48 (2016) 285–309, <https://doi.org/10.1146/annurev-fluid-122414-034425>.
- [44] S. Tcholakova, N.D. Denkov, I.B. Ivanov, B. Campbell, Coalescence in  $\beta$ -lactoglobulin-stabilized emulsions: Effects of protein adsorption and drop size, *Langmuir* 18 (2002) 8960–8971, <https://doi.org/10.1021/la0258188>.
- [45] H.H.J. De Jongh, H.A. Kosters, E. Kudryashova, M.B.J. Meinders, D. Trofimova, P. A. Wierenga, Protein Adsorption at Air-Water Interfaces: A Combination of Details, *Biopolymers* 74 (2004) 131–135, <https://doi.org/10.1002/bip.20036>.
- [46] Q. Brosseau, J. Vignon, J.C. Baret, Microfluidic Dynamic Interfacial Tensiometry ( $\mu$ DIT), *Soft Matter* 10 (2014) 3066–3076, <https://doi.org/10.1039/c3sm52543k>.
- [47] Y. Chen, C.S. Dutcher, Size dependent droplet interfacial tension and surfactant transport in liquid-liquid systems, with applications in shipboard oily bilgewater emulsions, *Soft Matter* 16 (2020) 2994–3004, <https://doi.org/10.1039/c9sm01892a>.
- [48] K. Wang, Y.C. Lu, J.H. Xu, G.S. Luo, Determination of Dynamic Interfacial Tension and Its Effect on Droplet Formation in the T-Shaped Microdispersion Process K, *Langmuir* 25 (2009) 2153–2158, <https://doi.org/10.1021/la803049s>.
- [49] N.J. Alvarez, L.M. Walker, S.L. Anna, A microtensiometer to probe the effect of radius of curvature on surfactant transport to a spherical interface, *Langmuir* 26 (2010) 13310–13319, <https://doi.org/10.1021/la101870m>.
- [50] H. Zhou, Y. Yao, Q. Chen, G. Li, S. Yao, A facile microfluidic strategy for measuring interfacial tension, *Appl. Phys. Lett.* 103 (2013), <https://doi.org/10.1063/1.4838616>.
- [51] H. Feng, D. Ershov, T. Krebs, K. Schroen, M.A.A. Cohen Stuart, J. Van Der Gucht, J. Sprakel, Manipulating and quantifying temperature-triggered coalescence with microcentrifugation, *Lab on a Chip* 15 (2015) 188–194, <https://doi.org/10.1039/c4lc00773e>.
- [52] M. Dudek, D. Fernandes, E. Helno Herø, G. Øye, Microfluidic method for determining drop-drop coalescence and contact times in flow, *Colloids Surfaces A Physicochem. Eng. Asp.* 586 (2020), <https://doi.org/10.1016/j.colsurfa.2019.124265> 124265.
- [53] T. Fu, Y. Ma, H.Z. Li, Bubble coalescence in non-Newtonian fluids in a microfluidic expansion device, *Chem. Eng. Process. Process Intensif.* 97 (2015) 38–44, <https://doi.org/10.1016/j.cep.2015.08.008>.
- [54] L. Yang, K. Wang, J. Tan, Y. Lu, G. Luo, Experimental study of microbubble coalescence in a T-junction microfluidic device, *Microfluid. Nanofluidics*. 12 (2012) 715–722, <https://doi.org/10.1007/s10404-011-0912-4>.
- [55] T. Segers, D. Lohse, M. Versluis, P. Frinking, Universal Equations for the Coalescence Probability and Long-Term Size Stability of Phospholipid-Coated Monodisperse Microbubbles Formed by Flow Focusing, *Langmuir* 33 (2017) 10329–10339, <https://doi.org/10.1021/acs.langmuir.7b02547>.